ASAP: Super-Contrast Vasculature Imaging Using Coherence Analysis and High Frame-Rate Contrast Enhanced Ultrasound

Antonio Stanziola, Chee Hau Leow, Eleni Bazigou, Peter D. Weinberg, and Meng-Xing Tang

***Abstract*— The very high frame rate afforded by ultrafast ultrasound, combined with microbubble contrast agents, opens new opportunities for imaging tissue microvasculature. However, new imaging paradigms are required to obtain superior image quality from the large amount of acquired data while allowing real-time implementation. In this paper, we report a technique–acoustic subaperture processing (ASAP)–capable of generating very high contrast/signal-to-noise ratio (SNR) images of macro- and microvessels, with similar computational complexity to classical power Doppler (PD) imaging. In ASAP, the received data are split into subgroups. The reconstructed data from each subgroup are temporally correlated over frames to generate the final image. As signals in subgroups are correlated but the noise is not, this substantially reduces the noise floor compared to PD. Using a clinical imaging probe, the method is shown to visualize vessels down to 200 μm with a SNR of 10 dB higher than PD and to resolve microvascular flow/perfusion information in rabbit kidneys noninvasively *in vivo* at multiple centimeter depths. With careful filter design, the technique also allows the estimation of flow direction and the separation of fast flow from tissue perfusion. ASAP can readily be implemented into hardware/firmware for real-time imaging and can be applied to contrast enhanced and potentially noncontrast imaging and 3-D imaging.**

***Index Terms*— Ultrasound, vascular imaging, contrast, SNR, coherence, microbubbles, in vivo.**

I. Introduction

ULTRASOUND is one of the most used front-line clinical imaging modalities, characterized by its real-time capability and excellent safety, affordability, and accessibility.

A recent advance in medical ultrasound (US) imaging is the successful development of high frame-rate (HFR) US imaging systems for both clinical applications and research [1]. HFR US acquires image by transmitting a plane/diverging wave covering the full field of view instead of the line by line sweeping in conventional US. The technique allows frame rates of tens of thousands of images per second and has been applied, for example, to soft tissue elastography [2], cardiac imaging [3], blood flow velocity mapping [4], and brain functional imaging [5].

Despite the obvious advantages of HFR US, its lack of focusing reduces both the signal-to-noise ratio (SNR) of the final image and its contrast, a problem which has been addressed for example by coherently compounding images acquired with different steering angles in transmission, at the expenses of the frame-rate [6]. The SNR problem is more challenging to solve when imaging blood vessels, due to the low echogenicity of red blood cells and the inability to coherently average many frames because the blood is moving [7].

The advent of microbubble contrast agents for contrast-enhanced ultrasound imaging (CEUS) has revolutionized the way that blood flow and perfusion can be imaged [8]. These micron-sized gas filled bubbles can provide significant signal enhancement from the blood. Various signal processing techniques have been developed in order to achieve highly sensitive, specific and quantitative imaging of the bubbles [9]–[11]. CEUS has shown great potential in the diagnosis and management of a range of cardiovascular diseases and cancer, and is gaining increasing acceptance in clinical practice [8], [12]. Furthermore, the shells of the bubbles can be chemically modified to target specific molecules of interest on the vascular endothelial surface, achieving ultrasound targeted/molecular imaging [13] and promising the detection of diseases at their earliest stage. More recently CEUS combined with signal processing has broken the wave diffraction limit and generated super-resolution images of vasculature at centimeter depth in vivo [14], [15].

The combined use of HFR imaging with CEUS opens new opportunities for imaging blood flow. The large amount of data acquired at high frame rates and the high sensitivity offered by CEUS can be used not only to better observe fast moving targets, such as hearts and arterial flow, but also to produce images of superior quality by condensing information from multiple frames while maintaining real-time frame rates in display [16]. In this area, signal processing methods are being designed to take advantage of the improved technology. For example, in [17], 2D flow velocity is recovered by estimating the displacement of the speckle pattern given by microbubbles

Manuscript received December 19, 2017; accepted January 11, 2018. Date of publication February 28, 2018; date of current version July 31, 2018. The work of A. Stanziola was supported by a Bioengineering Departmental Ph.D. Scholarship. The work of C. H. Leow and M.-X. Tang was supported in part by the EPSRC under Grant EP/M011933/1 and in part by the CRUK Multidisciplinary Project Award under Grant C53470/A22353. The work of E. Bazigou and P. D. Weinberg was supported by the British Heart Foundation under a programme grant. *(Corresponding author: Meng-Xing Tang.)*

The authors are with the Bioengineering Department, Imperial College London, London SW7 2AZ, U.K. (e-mail: antonio.stanziola14@imperial.ac.uk; mengxing.tang@imperial.ac.uk).

Color versions of one or more of the figures in this paper are available online at http://ieeexplore.ieee.org.

Digital Object Identifier 10.1109/TMI.2018.2798158

using a cross correlation approach, thanks to the high frame-rate which reduces speckle decorrelation between consecutive frames. In a similar way, the speckle pattern of clutter has been used in [18] to provide adaptive clutter filtering which reduces the smallest detectable velocity in Power Doppler images. Tremblay-Darveau *et al.* [19] use Color and Power Doppler to extract flow information at both arterial and capillary level, exploiting the frequency shift of the second harmonic Doppler signal during pulse inversion. Other laboratory-based studies are exploiting HFR CEUS to estimate blood flow and mixing in large vessels, using bubble destruction [20]. Also, Singular Value Decomposition has been exploited to separate clutter and vascular signals in the beamformed images [21], [22].

While there are many opportunities in the clinical application of HFR CEUS, a key challenge is the requirement for both effective and computationally efficient methods for processing the large quantity of data acquired (typically ∼1 Gbyte per second) that can produce superior image quality. Also, while microbubbles increase the strength of the echoes from inside blood vessels, the increase is frequency dependent [23]: at higher clinical frequencies, the weaker signal from existing commercial contrast agents still poses challenges in terms of SNR at depth, and requires methods for processing HFR US data to improve image SNR. For imaging blood flow without contrast agents the SNR challenge is even greater.

Recently, a few methods have used signal coherence to enhance the sensitivity of Doppler. For example, Li and Dahl [24] use spatial (fast-time or depth) correlation between transducer channel pairs, to extract the Doppler signal. They also show that the noise is uncorrelated between channels, a principle also used in our work. Their work is based on short lag spatial coherence (SLSC) imaging [25] and shows promising results, although it is computationally demanding, suffers from spatial blurring and has a minimum achievable SNR dictated by the number of channel lags used [26].

In [27], noise suppression is achieved by imaging the magnitude of the first lag autocorrelation of the Doppler signal. This is very promising, but has limitations with interference-reduction methods such as compounding, due to the rotation of the point spread function between consecutive frames, which will create spurious correlations or increase the minimum lag at which the correlation is measured. A more detailed analysis of the lagged correlation methods is given in [28].

In [29] Seo and Yen try to reduce the effect of interference noise by applying different apodization to the transducer, followed by a correlation in the depth direction (fast time), following an idea substantially similar to SLSC, but where each channel is in fact the beamformed result of different apodizations. The result of such an operation is used as a weight for the pixel intensity, creating a technique called Dual Apodization with Cross-Correlation (DAX). A more recent review of DAX and derived methods is in [30]: here, it is also shown using a k-space argument why the grating lobes between two images, made with alternating pattern apodizations, have opposite phase.

In this study, we try to improve image SNR by developing a new imaging technique, Acoustic Sub-Aperture Imaging (ASAP), as a fast and robust way of generating high contrast vascular images from HFR CEUS data, taking advantage of the large quantity of data available: in particular, we look at the coherence of samples between channels over different image frames, rather than in depth or over different compounded angles.

In our method, we split the data received from the ultrasound transducer into two sets, as in DAX: for each set, an image sequence is reconstructed. Supported by the large number of frames recorded by HFR US, we measure the signal coherence in slow time, directly on the classically defined Doppler signal. This exploits the lack of correlation of noise between the image sequences to reduce the noise level, and hence to enhance the contrast of the reconstructed vascular structures. The processing is done by multiplying the two images and averaging the result across a given number of frames, effectively performing cross-correlation. The computational complexity of the approach is essentially equal to Power Doppler. Moreover, it does not require any hardware modification and can be readily implemented via software upgrade into any scanner that uses digital beamforming. The method has been tested using CEUS scans, although its principles do not assume any particular characteristic of the response of the scatterers.

II. Principles of ASAP

A. Power Doppler

For each frame F of an HFR US sequence, a set of radiofrequency signals (one for each channel) is acquired. There are various methods to reconstruct an ultrasound image from such data. We will focus on delay and sum (DAS) beamforming, where each pixel of the final image is calculated independently. Focusing on a single pixel location, the method works by sampling the waveform of each channel i at a specific time-point given by the beamforming delays, to obtain an estimation of the acoustic signal recorded by such channel $b_i(F)$. Here F explicitly indicates that such a value depends on the frame considered.

Calling $\mathbf{b}(F) = [b_1(F)\, b_2(F) \ldots b_N(F)]$ the vector of samples extracted from each channel, the second step of DAS requires the summation of all those samples to obtain a single value for each frame. This is equivalent to defining a vector w all made of ones and calculating $p(F) = \boldsymbol{w}^T \mathbf{b}(F)$. The sequence $p(F)$ represents, for the pixel of interest, what is usually called the Doppler signal when imaging blood flow [31].

The signal coming from blood scatters such as red blood cells or microbubbles must be differentiated from tissue signal to produce a vascular image. For this purpose, we filter the Doppler signal obtained for each pixel with a high-pass filter in order to attenuate slow moving tissue artefacts.

In this paper, as we are dealing with CEUS scans, we also use Pulse Inversion (PI) to attenuate the signal coming from tissue while preserving contrast agent harmonics [11]. This is, however, a step to further improve the tissue rejection of CEUS scans and is not mandatory for the ASAP method.

Taking the power of each pixel signal, over frames, is what is usually called Power Doppler (PD):

$$\begin{aligned} PD &= \sum_{F=1}^{M} p(F)\overline{p(F)} = \sum_{F=1}^{M} \boldsymbol{w}^T \boldsymbol{b}\,(F)\,\boldsymbol{b}^T\,(F)\,\boldsymbol{w} \\ &= \boldsymbol{w}^T \left[\sum_{F=1}^{M} \boldsymbol{b}\,(F)\,\boldsymbol{b}^T\,(F)\right] \boldsymbol{w} \\ &= \boldsymbol{w}^T R \boldsymbol{w}, \end{aligned} \tag{1}$$

where M is the number of frames used.

The matrix $R \in \mathrm{C}^{N\times N}$ is obtained by cross-correlating each pair of channels over frames F. Treating each $b_i(F)$ as a random variable b_i measured at different frames F, and assuming that we process a large enough number of frames, each entry of the matrix is $R_{i,j} \simeq \mathrm{E}[b_i \overline{b_j}]$. Here the expectation E is evaluated over different frames.

If the recorded signals are corrupted by uncorrelated noise with variance σ_n, the matrix R can be decomposed as $R = S + R_i + \sigma_n I$, with S equal to the signal correlation matrix, R_i is the interference correlation and I the identity matrix. The knowledge of this matrix can be used in several ways to improve image quality. To give an example among many, if we are interested in reducing interference, the correlation matrix could be used (and indeed is very suited) for calculating the apodization according to the minimum variance method, by substituting it to the classical sample covariance matrix [32].

Our goal in this study, however, is to reduce the contribution of electronic and uncorrelated noise in the final image, without requiring the time consuming explicit calculation of the covariance matrix. Assuming noise between channels is not correlated, it only contributes to the diagonal entries of the cross correlation matrix R.

B. Acoustic Sub-Aperture Processing (ASAP)

To reduce the noise which exists only in the diagonal entries of the correlation matrix R, we beamform the signals using two different, non-overlapping apertures represented by the vectors $\boldsymbol{w}_1$ and $\boldsymbol{w}_2$. The vectors $\boldsymbol{w}_1$ and $\boldsymbol{w}_2$ are complementary and made of ones and zeroes. If we correlate the Doppler signals obtained by those two apertures, neglecting interference noise for simplicity, we will estimate the following value

$$ASAP = \boldsymbol{w}_1^T R \boldsymbol{w}_2 = \boldsymbol{w}_1^T S \boldsymbol{w}_2 + \boldsymbol{w}_1^T\,(\sigma_n I)\,\boldsymbol{w}_2, \tag{2}$$

but because the two apertures are non-overlapping, the result simplifies to

$$ASAP = \boldsymbol{w}_1^T S \boldsymbol{w}_2. \tag{3}$$

Note that this is fundamentally different than what happens in PD, in which a single apodization $\boldsymbol{w}$ is used. Assuming for simplicity that $\boldsymbol{w}$ is made of all ones, the estimated output is

$$PD = \boldsymbol{w} R \boldsymbol{w} = \boldsymbol{w} S \boldsymbol{w} + \boldsymbol{w}\,(\sigma_n I)\,\boldsymbol{w} = \boldsymbol{w} S \boldsymbol{w} + N\sigma_n \tag{4}$$

where noise clearly contributes to the final value.

All previously given results are true in the limit of an infinite number of samples. For a finite number of frames the SNR improvement of ASAP (with respect to Gaussian noise) will be proportional to the square root of the number of frames. Note also that more than two apertures can be used by correlating them in pairs and averaging the result.

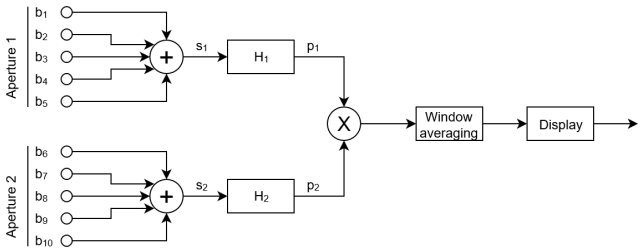

Fig. 1. Schematic of the ASAP method. For each pixel, data coming from different channels b_i is split in two apertures and beamformed, to generate the signals s_i . Such signals are then filtered individually by filters H, and then multiplied and averaged to perform cross correlation. The result is then processed to remove unwanted signal such as sidelobes, log compressed and displayed.

For the results presented in this paper, the apertures are made by alternately placing four consecutive channels in one of the two groups. This choice is justified later in the Results section.

The interesting point of this approach is that the calculation of the matrix R is not necessary. It is just necessary to beamform two images with half of the channel each. In this way, the method has practically the same computational complexity as PD.

A diagram showing how ASAP is performed can be seen in Fig. 1.

C. Display of Results

In contrast to the Power Doppler signal, which is real and positive by definition, the ASAP cross-correlation is a generic complex scalar. The phase of this number is important, as we expect a real and positive number (i.e. phase zero) from the source of interest.

Various methods can be envisaged to penalize cross-correlations with a phase other than zero: in this paper, we will just display the real part of the cross correlation and set any negative correlation values to zero as it corresponds to interference, for example from side lobes: throughout this paper, we will denote as interference signals the contribution given by side and grating lobes. Power values and their SNR are always shown as 10log10(x), while amplitudes are show as 20log10(x).

D. Wall Filtering and Flow Direction Estimation

The easiest way to apply a wall filter is to use the same filter on both apertures. This will naturally behave like a classical wall filter applied on a Doppler signal, because of the linearity of the filtering process.

To clarify how wall filtering the two apertures affects the ASAP signals, we will restrict our analysis to the noise-free signal. With such a simplification, calling $P_i(f)$ the Doppler spectrum of the signal from the i-th aperture, the zero-lag cross

correlation between two of them (i.e. the ASAP signal) is

$$\sum_F p(F)\overline{p(F)} = \int_{-f_N}^{+f_N} P_1(f)\,\overline{P_2(f)}\,df$$
$$= \int_{-f_N}^{+f_N} \|S(f)\|^2 \cdot H_1(f)\,\overline{H_2(f)}\,df, \quad (5)$$

where $S(f)$ is the spectrum of the source signal, f_N is the Nyquist frequency and $H_i(f)$ is the filter applied on the i-th aperture.

The equation shows that the resulting filter is the product of the filters applied on each aperture. This allows design flexibility, for example by using a high-pass and a low-pass filter on the two apertures respectively to obtain an effective band-pass filter. It must be noted, however, that the phase of the two filters must be matched for the correlation to behave as usually expected.

In fact, zero-lagged cross correlation is simply the integral of the Power Spectrum, eventually filtered. By definition, the Power Spectrum is real and positive. If the two filters have matched phase, then eq. (5) reduces to

$$\int_{-f_N}^{+f_N} \|S(f)\|^2 \cdot \left\| H_1(f)\,\overline{H_2(f)} \right\| df \quad (6)$$

which shows that the two filters only act as real non-negative weights of each frequency bin, as expected. Conversely, if the phase of the two filters is not matched, the cross correlation operation reduces to

$$\int_{-f_N}^{+f_N} \|S(f)\|^2 \cdot e^{j\theta(f)} \left\| H_1(f)\,\overline{H_2(f)} \right\| df \quad (7)$$

where j is the imaginary unit and $\theta(f)$ is the phase mismatch of the two filters. In this case, the power spectrum is clearly not real and positive anymore, and therefore we are not performing a classical cross correlation.

Having a global filter with a phase different from zero can be used to infer information other than Power Doppler, while still taking advantage of the noise reduction. Depending of the goal, it may be convenient to design directly the global filter rather than the two initial ones.

As an example of using the phase in filter design, we will use two simple filters to extract the flow direction directly from the correlation value. We use two different filters on each aperture: a high pass, $[1\ -1]$, and a low pass $[1\ 1]$. The high-pass filter has a zero at the DC frequency, which creates a jump of π (i.e. a change of sign) in the phase spectrum between positive and negative frequencies, as visible in Fig. 2. This reduces the ASAP value to

$$ASAP = -\int_{-\infty}^{0} \|S(f)\|^2 \cdot \|H_1(f)\,H_2(f)\|\,df$$
$$+ \int_{0}^{+\infty} \|S(f)\|^2 \cdot \|H_1(f)\,H_2(f)\|\,df \quad (8)$$

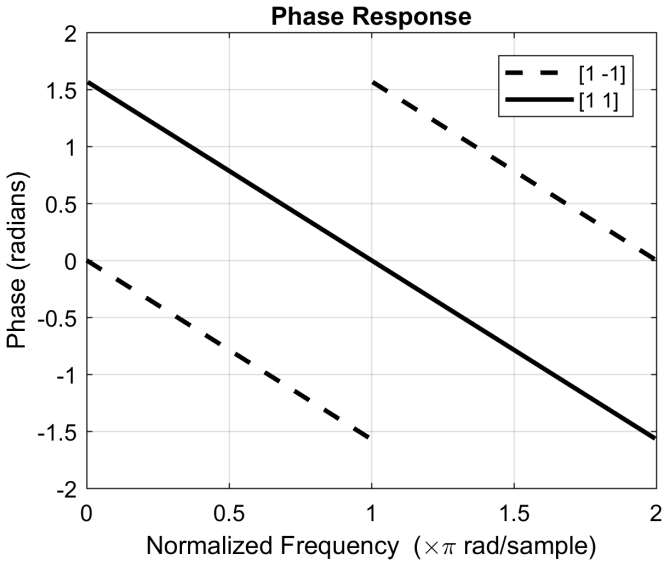

Fig. 2. Phase plot of the two filters used in the example of section II.D, which highlights the sign change in the middle of the spectrum.

The result will have a negative sign if the Doppler spectrum is concentrated in the negative frequencies and a positive sign in the opposite case. We therefore know the sign of the average frequency just by looking at the sign of the cross-correlation result, and therefore we can infer and display the direction of flow.

III. Methods

A. In-Vitro Experiments

To evaluate noise suppression, the cross-section of a 200μm tube containing flowing microbubbles was imaged using Pulse Inversion and processed using both ASAP and PD

The tube was located roughly 1.5cm below the transducer center. A suspension of 0.1mL of contrast agent (SonoVue, Bracco Imaging SpA, Milan, Italy) per liter of water was driven through the tube at a mean speed of 20cm/s by a syringe pump. The ultrasonic acquisition was performed using 4MHz single-cycle pulses at 0.2 MI from a L12-3v linear array probe and Vantage 128 ultrasound platform (Verasonics, Kirkland, WA, USA). The experiment used only the central 128 elements of the probe, for a total aperture width of roughly 2.5cm. Seven compounded plane-waves, equally spaced between -20 and $+20$ degrees, gave a final frame-rate of 875 Hz. The acquired RF data were filtered in fast-time (depth) using a 5th order Butterworth bandpass filter with cutoff frequencies at 6MHz and 12MHz. A total of 10 acquisitions has been done and the results averaged.

B. In-Vivo Experiments

The kidney of a healthy rabbit was imaged to assess its vasculature. All procedures complied with the Animals (Scientific Procedures) Act 1986 and were approved by the Local Ethical Review Process Committee of Imperial College London (Home Office Licence PPL 70/7333).

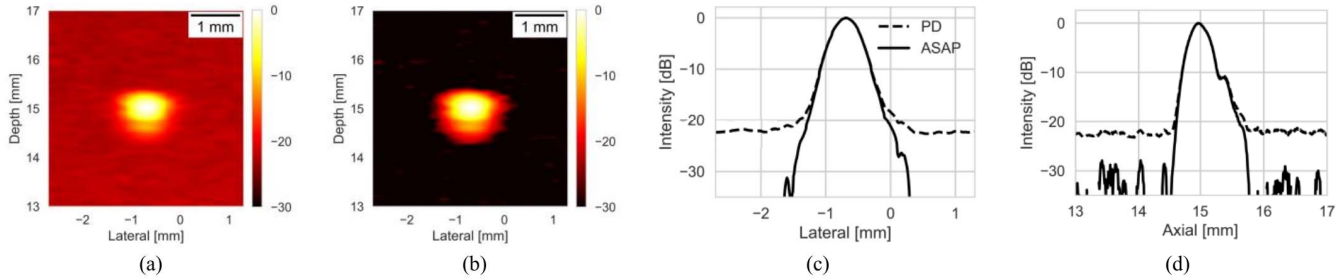

Fig. 3. In vitro results,showing the cross-section of a 200 micron diameter vessel with flowing microbubbles using Pulse Inversion Power Doppler (a) and ASAP (b) processing. Both images were made using 200 frames acquired over 0.22s. (c) and (d) show the lateral and axial plot, respectively, for the same acquisition.

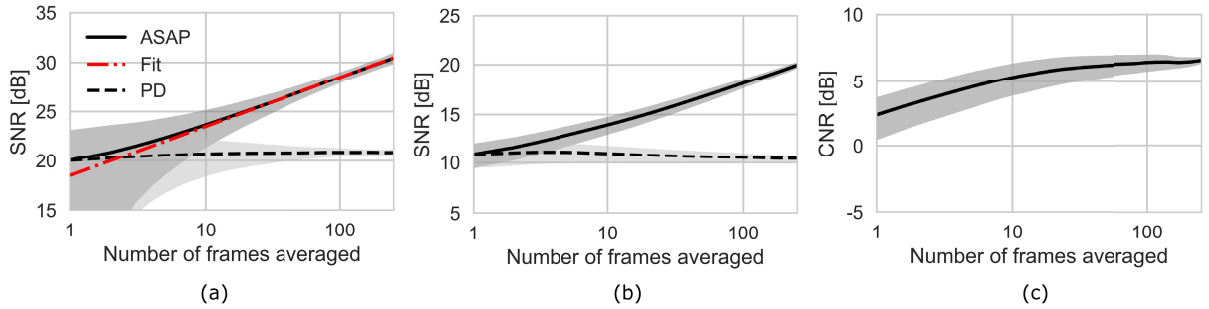

Fig. 4. Evolution of SNR as a function of the number of frames averaged, for in-vitro (a) and in vivo (b) experiments. The red line shows a square root fit. The plot in (c) shows the CNR evolution: the PD and ASAP lines are exactly overlapping. Axis are in logarithmic scale.

The male New Zealand White rabbit (6 months old; HSDIF strain, Specific Pathogen Free, Harlan UK) was anesthetized with medetomidine (0.25 mL/kg) and ketamine (0.15 mL/kg) while body temperature was maintained at 37C by a warming plate. A pulse oximeter (Edan VE-H100B) was attached to the tail to monitor oxygen saturation and heart rate. The fur around the scanning site was shaved to acquire images of the rabbit's right renal vasculature. SonoVue microbubbles were injected via the marginal ear vein as a bolus of 0.25 mL. The ultrasound acquisition was the same as the in-vitro experiment, except that each frame was reconstructed from 15 compounded angles between -18 and 18 degrees, with a final frame-rate of 750Hz. The data were transferred to a PC for offline processing using Matlab (The MathWorks, Natick, MA, USA).

C. Image Quality Measures

To evaluate the quality of ASAP images compared to PD, two measures have been adapted from [24].

The first one, Signal-to-noise ratio (SNR), gives an indication of the power of the signal of interest compared to noise power. It has been calculated in dB scale as

$$SNR = 10\log_{10}\left(\frac{\sqrt{E\left[I_s^2\right]}}{\sqrt{E\left[I_n^2\right]}}\right), \tag{9}$$

where I_s and I_n are the pixel intensities in the signal and noise region of interest, respectively, and the expectations are taken over all the pixels in the region of interest.

The second measure is Contrast to Noise Ratio (CNR) is given as

$$CNR = 10\log_{10}\left(\frac{|\mu_s - \mu_n|}{\sqrt{\sigma_s^2 + \sigma_n^2}}\right), \tag{10}$$

Where $\mu_s = E[I_s]$ and $\mu_n = E[I_n]$ are the mean value in the signal and noise region, respectively. Similarly, $\sigma_s^2 = E\left[I_s^2\right] - \mu_s^2$ and $\sigma_n^2 = E\left[I_n^2\right] - \mu_n^2$ are the variances of the pixel values across the signal and noise region.

IV. Results

A. Noise Rejection

Fig. 3 shows the ability of ASAP to substantially reduce the noise floor while maintaining image axial resolution. Since we are performing a correlation estimation, noise suppression will improve with the number of averaged frames. This is fundamentally different from what happens using PD, which is not able to distinguish between noise and Doppler signal power.

The ability of ASAP to improve the signal-to-noise ratio (SNR) as more frames are acquired is depicted in Fig. 4(a), where the SNR is plotted against number of frames. As expected, the noise floor in PD remained approximately constant at 21dB, even when ensemble averaging over 200 frames. On the other hand, processing with ASAP shows an improvement of 10dB compared to PD with 250frames used, with an improvement proportional to the square root of the number of frames used, as predicted by the theory, reaching an SNR of 31dB. The same behavior was observed for in-vivo experiments: Fig. 4(b) shows that an increase of 10dB in SNR was achieved by ASAP over PD.

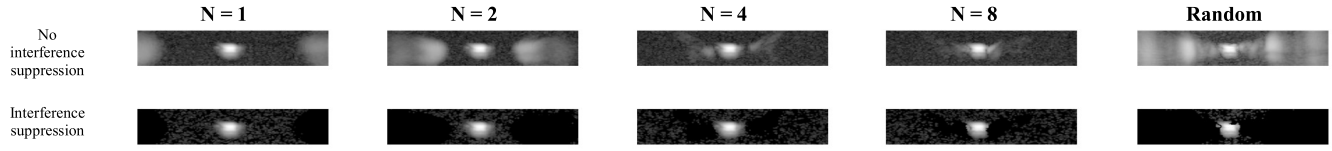

Fig. 5. Estimation of the point spread function obtained when using ASAP, by means of a tube with flowing microbubbles, imaged in cross section. The first row shows the result of ASAP when interference is not suppressed, for different apertures. The second row shows the effect of suppressing interference signals, by setting negative correlations to zero. The dynamic range of the images is 40dB, 1000 frames are averaged.

The CNR of ASAP, on the other hand, is similar to PD and its evolution with the number of frames exactly overlaps the PD one, as visible in Fig. 4 (c).

B. Choice of Sub-Apertures

The way channels are divided into two different groups affects the shape of the point spread function (PSF) given by each one of the two sub-apertures. This in turn changes the correlation of the interference signals, which are represented as side and grating lobes.

To evaluate this effect, we studied the PSF after processing the in-vitro data with ASAP using different sub-apertures. Apertures were chosen to have no overlapping elements to ensure noise decorrelation. In [29] it is shown that grouping the channels in two non overlapping apertures results into positively correlated mainlobe signals and negatively correlated interference lobes: with this in mind, negative correlating interference lobes can be detected and removed by setting the corresponding pixels to zero.

The channels were first subdivided into groups A_i of size N: for example, A_1 contained channels 1 to N. Then, the groups were allocated to sub-apertures. For example, channels belonging to groups with odd i were used for the first sub-aperture, while the others were used for the second. N is basically the number of contiguous channels used together in one aperture.

We investigated apertures with N equal to 1, 2, 4 and 8. We also randomly split the channels into two apertures. The results of ASAP processing for different apertures are shown in Fig. 5.

The first row of the image was obtained by taking the absolute value of the correlation without removing negative correlations. This creates artefacts in terms of grating- and side-lobes. The image shows how increasing N moves the interference lobes closer to the mainlobe.

In the second row, negative correlations were set to zero, and it can readily be seen that all interference signals have been suppressed. This confirms the expected negative correlation between side and grating lobes of the two apertures. The last column highlights how using random apertures performs poorly in terms of interference.

Fig. 6 shows the lateral plots for the images in Fig. 5. It can be seen that the apertures for N = 4 and 8 give weaker sidelobes. This is the preferred condition, as the negative correlation of strong interference signals can mask the signal coming from weaker scatters, even if noise has been sufficiently suppressed.

On the other hand, taking too large an N may affect the results in the immediate near-field of the transducer. That is

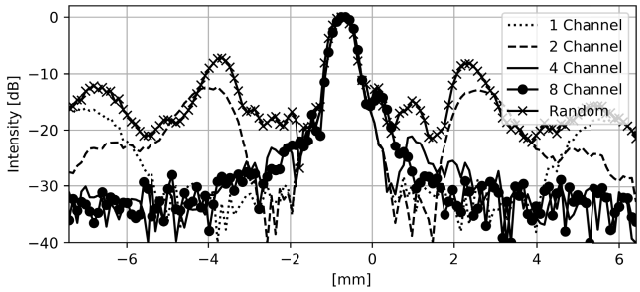

Fig. 6. Lateral plot of the PSF when different apertures are used, without interference suppression, showing the position and strength of the side and grating lobes.

because the signal of a near field scatter has strong intensity in only a few adjacent channels, which can end up all in the same sub-aperture, reducing the cross-correlation between the sub-apertures. For this reason, in this paper we use N = 4.

C. Vascular Imaging

To demonstrate the technique in vivo, the kidney of a healthy rabbit was scanned. In the resulting Pulse Inversion image (Fig. 7a), some of the non-contrast structures were still visible due to nonlinear propagation artefacts [33]. It is also difficult to understand the vascular morphology because of speckle noise. The latter effect was mitigated by averaging several frames incoherently, after envelope extraction, to smooth the speckle noise for moving targets (Fig. 7b). Although this may help in delineating the main vascular structure, in practice it was necessary to use a wall filter and perform PD imaging (Fig. 7c). (Note that in our experiments the wall filter is always used after PI summation, for both PD and ASAP.)

Despite improvements in the image quality, the noise floor was high and comparable to the weak signals coming from some of the smaller vessels, especially in the deep regions of the image. As the noise power often changes with depth (because of depth varying signal amplification upon reception, also known as TGC), it is hard to separate noise from the fainter vessels by varying the dynamic range. This is especially true in real-time imaging, when the variance of PD is high due to the small number of frames used in the estimation. Using our technique, which generated the image shown in Fig. 7d, the noise level is largely reduced and the vasculature contrast is enhanced, especially in the challenging parts of the image. The rapid improvement in SNR with number of frames also makes possible the quantification of flow dynamics: we give an example, with the signal power

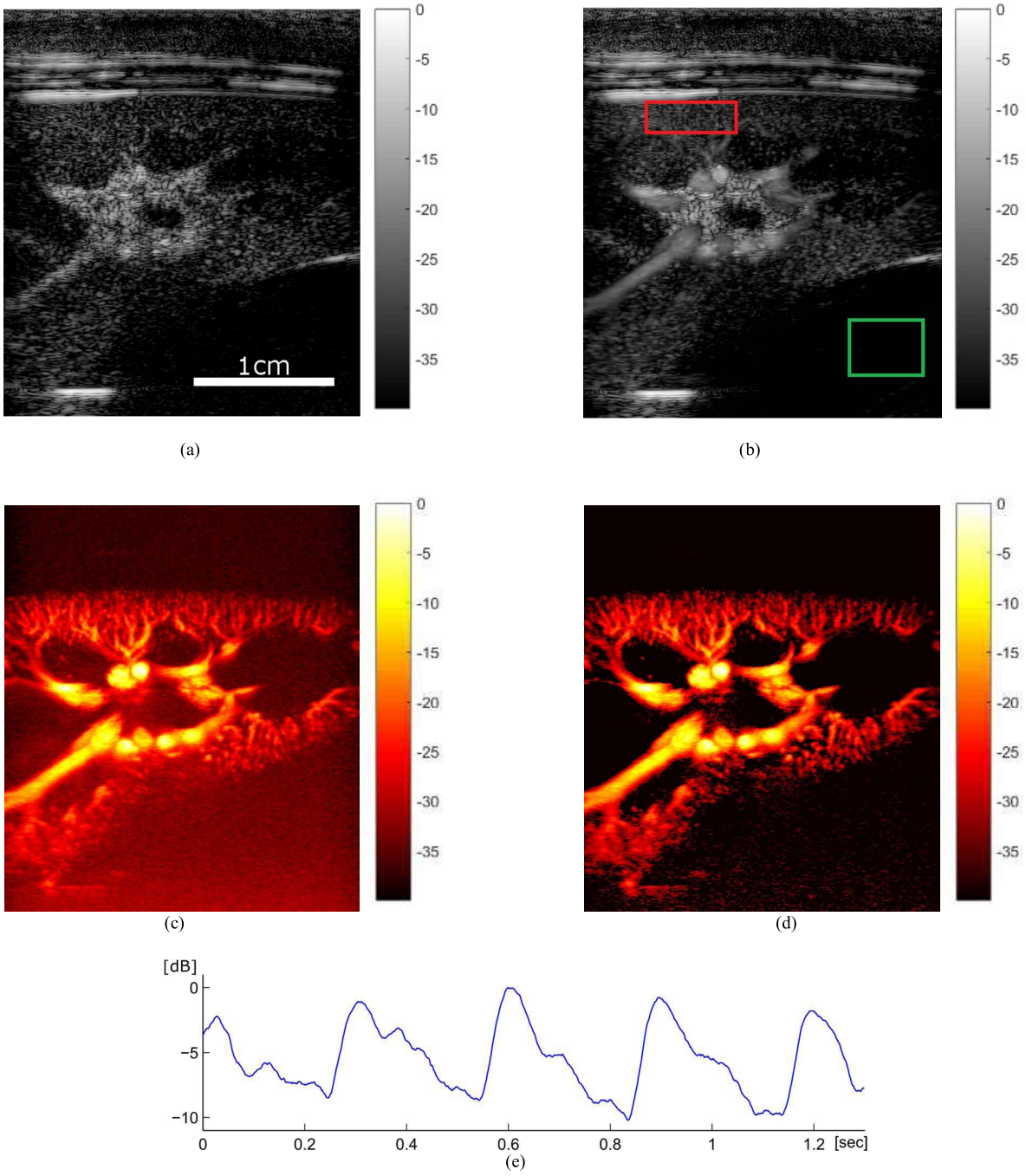

Fig. 7. In-vivo acquisition of a rabbit kidney after bolus injection of microbubbles: Pulse Inversion (a) and incoherent averaging (b), Power Doppler (c) and ASAP processing (d), displayed at 40dB of dynamic range. Averaging is done over 0.05sec, giving an imaging frame rate of 20Hz, for images (b), (c) and (d). Image (e) shows the quantification of flow dynamics in the upper cortical region. The image in (b) also shows the region used for signal (red ☐) and noise (green ☐) measurement in SNR estimation.

in the cortex region, in Fig. 7e. The resulting image enhancement makes the technique suitable for producing high-contrast images of the vasculature in real time[1].

D. Separation of Macro- and Micro-Flow Using Wall Filter

As mentioned, HFR US acquires thousands of frames per second, generating gigabytes of data; a processing technique that is computationally demanding therefore reduces the feasibility of real-time implementation. ASAP can be fully parallelized in a pixel-wise manner, without increasing the computational workload compared to the classical Power Doppler estimation. To further reduce complexity, we propose the use of a simple 2 tap Finite Impulse Response (FIR) filter, which is the backward finite difference: that is, we simply subtract consecutive frames. Although a filter with such a short impulse response has a poor transition at the cut-off frequency, the use of high frame rate imaging makes slow-moving signals very close to the zero-frequency, allowing simpler filters to be used. It must be noted that the use of such filters is not

[1]Supplementary materials are available in the supporting documents / multimedia tab

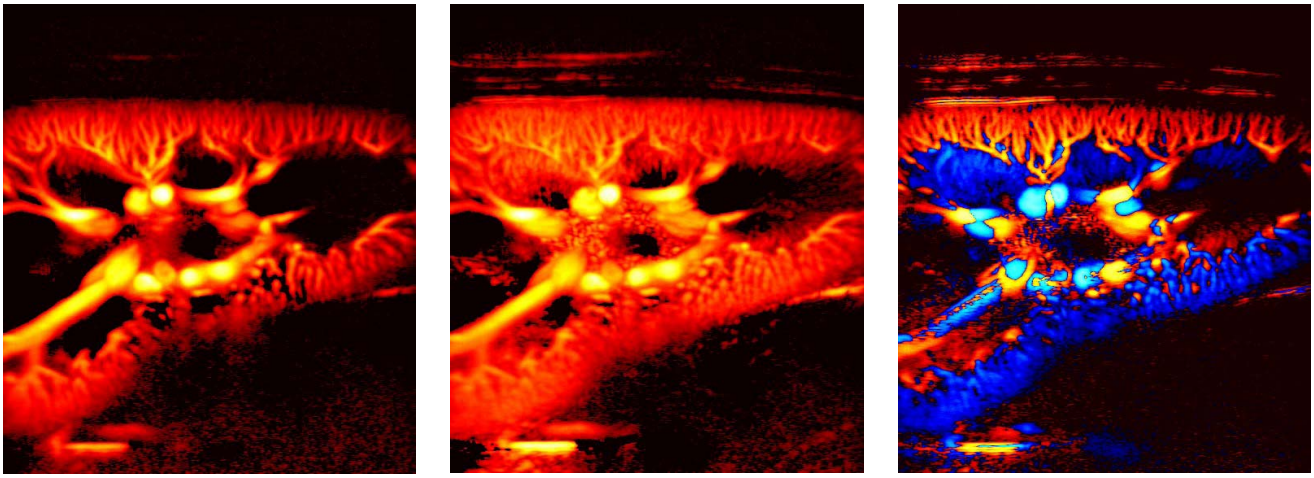

(a) (b) (c)

Fig. 8. Results for different wall filters. Images (a) and (b) show the effects of a different lag between the two subtracted images, analyzed using ASAP. The first image has a cut-off frequency of $f = 187$Hz, corresponding to a vertical blood velocity of $v = 36$mm/s, the second one of $f = 31$Hz or $v = 6$mm/s. The image in (c) shows the ability to discriminate different flow directions. Dynamic range is 50dB, averaging over 1000 frames (about 1.3 sec), corresponding blood vertical velocity is calculated with respect to the transmitted frequency.

fundamental to the ASAP technique. The direct difference of two consecutive frames has already been evaluated for the transverse oscillation method and proved promising for fast flow evaluation [34].

We extend it by varying the temporal distance between the two frames being subtracted. This changes the lowest cut-off frequency of the filter, highlighting vessels with different flow speed. An example is shown in Fig. 8a and Fig. 8b. It can clearly be seen that increasing the lag between the two subtracted frames allows more microvessels to be seen, especially ones in which microbubbles flow from the kidney cortex to the pyramid. We can therefore effectively lower our cut-off frequency, i.e. evaluate different flow regimes, while maintaining the same computational load. Another possibility is to use different filters for each one of the signals being correlated.

Following the example given at the end of Sec. II, we used two filters to obtain information on flow direction from the correlation value. This is illustrated in Fig. 8c, where flow towards the transducer is shown in red and flow moving away from the transducer is in blue[2].

V. Discussion

In this paper, we propose an ultrasound imaging method, Acoustic Sub-Aperture Processing, capable of generating very high contrast images (with up to 10dB improvement over existing Doppler techniques both in-vitro and in-vivo) of macro- and microvessels in vivo at multi-centimetre depth, taking advantage of high frame-rate ultrasound and microbubble contrast agents.

The results show that CNR measures for ASAP are similar to PD. Actually they overlap as shown in Fig. 4(c). This is due to the fact that CNR measures take into account variance in the regions of interest, and for both PD and ASAP the local variance decreases with number of frames used. However it should be noted that such a measure in a local region does not account for the global variations of noise in the ultrasound images; noise is known which is known to change over imaging depth, as can be seen in Fig. 7 (c). PD can only reduce local noise variations through local averaging but cannot reduce global variations of noise, while ASAP can reduce the noise mean close to zero globally if a sufficient number of frames are used.

By adjusting the signal processing chain, flow of different speeds and direction could also be separated. Having such a rapid reduction of the noise floor increases the ability to detect small vessels while maintaining the image frame rate for real-time applications.

From an implementation point of view, during PD the output of a single pixel is squared by multiplying it by its own conjugate. The only practical difference in our approach is that the multiplication is performed with two different numbers, belonging to two different beamforming outputs. The computational load of this parallel process is therefore the same as for PD, meaning that real-time implementation is achievable, requiring only a minimal upgrade of the machine, and possibly involving only software changes if digital beamforming is used.

The way we choose our apertures, $\boldsymbol{w}_1$ and $\boldsymbol{w}_2$, and our vector of samples b, affects the quality of the final image and its noise suppression. So far, we have populated our vector b by sampling each channel at the time given by the delay and sum algorithm. For example, our apertures have been chosen by alternately placing four consecutive channels in one of the two groups.

It has been shown that grouping channels in two non-overlapping apertures is likely to create interference signals, in the form of side and grating lobes, which are negatively-correlated between the two groups [29]: such effects and their potential impact on the image have to be taken into account when apertures are chosen. This is because, while the sign of

[2]Supplementary materials are available in the supporting documents / multimedia tab

the correlation helps differentiate between main and side-lobe signals, strong interference may mask the signal coming from a weak target next to a strong one.

The results show that, in general, increasing the number of adjacent channels in each group moves the interference pattern closer to the main lobe. On the other hand, a great reduction in the number of neighboring channels used in each aperture will increase the grating-lobes while weakening the side-lobes: in the extreme case, where channels are used alternately in each aperture (i.e. odd channels in the first aperture and even channels in the second one), the result is effectively similar to using two transducers with doubled pitch. Approximate estimation of the result of a given choice of aperture can easily be computed using k-space methods [35], especially for linear targets.

To mitigate such effects, other ways of grouping the samples can be used, such as selecting different time instants of the waveform for each group. For example, assuming that the Born approximation holds and no non-linear scatterers are present (i.e. we are not using microbubbles), we could correlate the signal beamformed on each pixel with the one half a wavelength below in the depth direction. As the transmitted wave is known, the expected correlation between such signals is known as well, and ASAP can therefore be used.

Stanziola and Tang [36] have also shown that this method works by correlating pixels belonging to the same point spread function after beamforming, in image sequences after envelope detection (B-mode images), and it is therefore a good candidate for a post-processing method to increase the quality of PD acquisitions. A combination of both methods could be used to improve noise suppression and enhance the quality of the final image. The number of apertures can also be increased and their combined cross-correlation calculated in different ways.

ASAP's can also be combined with other methods for reducing side and grating lobes, such as DAX beamforming [37], [38], where the transducer aperture is also divided into sub-apertures to increase the quality of B-mode images, and minimum variance beamforming methods [39].

Lastly, we note that a trivial implementation of the technique may give undesirable results when imaging targets at very large depths or in the presence of strong aberration. Such situations may in fact change the steering vector associated with targets (delays) and, therefore, signals of interest may be misinterpreted as interference, as happens in classical minimum variance beamforming; this will result in a weaker signal. While the results presented are promising, as they are generated using a clinical probe, we speculate that in the aforementioned situations a more sophisticated or adaptive way of choosing the apertures may be necessary. This will be the subject of future studies. However, as we are using a clinical linear probe, the technique could be readily applied to those applications currently suitable for such linear probes, particularly for imaging small/micro-vasculatures in e.g. breast, head and neck, and small body parts.

The ability to image small vessel flow with good contrast, resolution and penetration depth (centimetres) in vivo, using an affordable and portable/accessible technology such as ultrasound, could be of great value. It could be used to detect subtle changes that are relevant to early detection/characterisation in cancer, as well as treatment monitoring and evaluation, in transcranial ultrasound imaging of brain function (where signal to noise ratio is very poor due to skull attenuation), and in the evaluation of organ perfusion during transplantation.

ACKNOWLEDGMENT

The authors would like to thank Dr. Robert Eckersley and his group, the late Professor David Cosgrove, and the whole ULIS group for their valuable advice during the realization of this work.

REFERENCES

[1] M. Tanter and M. Fink, "Ultrafast imaging in biomedical ultrasound," *IEEE Trans. Ultrason., Ferroelect., Freq. Control*, vol. 61, no. 1, pp. 102–119, Jan. 2014.

[2] L. Sandrin, S. Catheline, M. Tanter, X. Hennequin, and M. Fink, "Time-resolved pulsed elastography with ultrafast ultrasonic imaging," *Ultrason. Imag.*, vol. 21, no. 4, pp. 259–272, Oct. 1999.

[3] M. Cikes, L. Tong, G. R. Sutherland, and J. D'hooge, "Ultrafast cardiac ultrasound imaging: Technical principles, applications, and clinical benefits," *JACC Cardiovascular Imag.*, vol. 7, no. 8, pp. 812–823, 2014.

[4] M. Lenge, A. Ramalli, E. Boni, H. Liebgott, C. Cachard, and P. Tortoli, "High-frame-rate 2-D vector blood flow imaging in the frequency domain," *IEEE Trans. Ultrason., Ferroelect., Freq. Control*, vol. 61, no. 9, pp. 1504–1514, Sep. 2014.

[5] C. Errico, B. F. Osmanski, S. Pezet, O. Couture, Z. Lenkei, and M. Tanter, "Transcranial functional ultrasound imaging of the brain using microbubble-enhanced ultrasensitive Doppler," *Neuroimage*, vol. 124, pp. 752–761, Jan. 2016.

[6] G. Montaldo, M. Tanter, J. Bercoff, N. Benech, and M. Fink, "Coherent plane-wave compounding for very high frame rate ultrasonography and transient elastography," *IEEE Trans. Ultrason., Ferroelect., Freq. Control*, vol. 56, no. 3, pp. 489–506, Mar. 2009.

[7] B. Denarie *et al.*, "Coherent plane wave compounding for very high frame rate ultrasonography of rapidly moving targets," *IEEE Trans. Med. Imag.*, vol. 32, no. 7, pp. 1265–1276, Jul. 2013.

[8] J. R. Lindner, "Microbubbles in medical imaging: Current applications and future directions," *Nature Rev. Drug Discovery*, vol. 3, no. 6, pp. 527–533, 2004.

[9] A. Stanziola, M. Toulemonde, Y. O. Yildiz, R. J. Eckersley, and M.-X. Tang, "Ultrasound imaging with microbubbles," *IEEE Signal Process. Mag.*, vol. 33, no. 2, pp. 111–117, Mar. 2016.

[10] R. J. Eckersley, C. T. Chin, and P. N. Burns, "Optimising phase and amplitude modulation schemes for imaging microbubble contrast agents at low acoustic power," *Ultrasound Med. Biol.*, vol. 31, no. 2, pp. 213–219, Feb. 2005.

[11] D. H. Simpson, C. T. Chin, and P. N. Burns, "Pulse inversion Doppler: A new method for detecting nonlinear echoes from microbubble contrast agents," *IEEE Trans. Ultrason., Ferroelect., Freq. Control*, vol. 46, no. 2, pp. 372–382, Mar. 1999.

[12] D. Cosgrove and C. Harvey, "Clinical uses of microbubbles in diagnosis and treatment," *Med. Biol. Eng. Comput.*, vol. 47, no. 8, pp. 813–826, 2009.

[13] A. L. Klibanov, "Ligand-carrying gas-filled microbubbles: Ultrasound contrast agents for targeted molecular imaging," *Bioconjug. Chem.*, vol. 16, no. 1, pp. 9–17, 2005.

[14] K. Christensen-Jeffries, R. J. Browning, M.-X. Tang, C. Dunsby, and R. J. Eckersley, "*In vivo* acoustic super-resolution and super-resolved velocity mapping using microbubbles," *IEEE Trans. Med. Imag.*, vol. 34, no. 2, pp. 433–440, Feb. 2015.

[15] C. Errico *et al.*, "Ultrafast ultrasound localization microscopy for deep super-resolution vascular imaging," *Nature*, vol. 527, no. 7579, pp. 499–502, 2015.

[16] J. Viti, R. J. Vor, N. de Jong, F. Guidi, and P. Tortoli, "Detection of contrast agents: Plane wave versus focused transmission," *IEEE Trans. Ultrason., Ferroelect., Freq. Control*, vol. 63, no. 2, pp. 203–211, Feb. 2015.

[17] C. H. Leow, E. Bazigou, R. J. Eckersley, A. C. H. Yu, P. D. Weinberg, and M.-X. Tang, "Flow velocity mapping using contrast enhanced high-frame-rate plane wave ultrasound and image tracking: Methods and initial *in vitro* and *in vivo* evaluation," *Ultrasound Med. Biol.*, vol. 41, no. 11, pp. 2913–2925, 2015.

[18] J. Tierney, C. Coolbaugh, T. Towse, and B. Byram, "Adaptive clutter demodulation for non-contrast ultrasound perfusion imaging," *IEEE Trans. Med. Imag.*, vol. 63, no. 9, pp. 1979–1991, Sep. 2017.

[19] C. Tremblay-Darveau, R. Williams, L. Milot, M. Bruce, and P. N. Burns, "Combined perfusion and doppler imaging using plane-wave nonlinear detection and microbubble contrast agents," *IEEE Trans. Ultrason., Ferroelect., Freq. Control*, vol. 61, no. 12, pp. 1988–2000, Dec. 2014.

[20] C. H. Leow *et al.*, "Microbubble void imaging: A non-invasive technique for flow visualisation and quantification of mixing in large vessels using plane wave ultrasound and controlled microbubble contrast agent destruction," *Ultrasound Med. Biol.*, vol. 41, no. 11, pp. 2926–2937, 2015.

[21] C. Demené *et al.*, "Spatiotemporal clutter filtering of ultrafast ultrasound data highly increases Doppler and fUltrasound sensitivity," *IEEE Trans. Med. Imag.*, vol. 34, no. 11, pp. 2271–2285, Nov. 2015.

[22] P. Song, A. Manduca, J. Trzasko, and S. Chen, "Ultrasound small vessel imaging with block-wise adaptive local clutter filtering," *IEEE Trans. Med. Imag.*, vol. 36, no. 1, pp. 251–262, Jan. 2016.

[23] M.-X. Tang and R. J. Eckersley, "Frequency and pressure dependent attenuation and scattering by microbubbles," *Ultrasound Med. Biol.*, vol. 33, no. 1, pp. 164–168, 2007.

[24] Y. L. Li and J. J. Dahl, "Coherent flow power doppler (CFPD): Flow detection using spatial coherence beamforming," *IEEE Trans. Ultrason., Ferroelect., Freq. Control*, vol. 62, no. 6, pp. 1022–1035, Jun. 2015.

[25] M. A. Lediju, G. E. Trahey, M. Jakovlijevic, B. C. Byram, and J. J. Dahl, "Short-lag spatial coherence imaging," in *Proc. IEEE Ultrason. Symp.*, Oct. 2010, pp. 987–990.

[26] A. Stanziola and M.-X. Tang, "Super contrast imaging using high frame-rate CEUS and spatial and temporal signal processing," in *Proc. 21st Eur. Symp. Ultrasound Contrast Imag.*, Rotterdam, The Netherlands, 2017, pp. 1–14.

[27] A. Bar-Zion, C. Tremblay-Darveau, O. Solomon, D. Adam, and Y. C. Eldar, "Fast vascular ultrasound imaging with enhanced spatial resolution and background rejection," *IEEE Trans. Med. Imag.*, vol. 36, no. 1, pp. 169–180, Jan. 2017. [Online]. Available: https://arxiv.org/abs/1601.05710v4, doi: 10.1109/TMI.2016.2600372.

[28] C. Tremblay-darveau *et al.*, "Improved contrast-enhanced Power Doppler using a coherence-based estimator," *IEEE Trans. Med. Imag.*, vol. 36, no. 9, pp. 1901–1911, Sep. 2017.

[29] C. H. Seo and J. T. Yen, "Sidelobe suppression in ultrasound imaging using dual apodization with cross-correlation," *IEEE Trans. Ultrason., Ferroelect., Freq. Control*, vol. 55, no. 10, pp. 2198–2210, Oct. 2008.

[30] J. Shin, Y. Chen, H. Malhi, and J. T. Yen, "Ultrasonic reverberation clutter suppression using multiphase apodization with cross correlation," *IEEE Trans. Ultrason., Ferroelect., Freq. Control*, vol. 63, no. 11, pp. 1947–1956, Nov. 2016.

[31] O. Bonnefous and P. Pesqué, "Time domain formulation of pulse-Doppler ultrasound and blood velocity estimation by cross correlation," *Ultrason. Imag.*, vol. 8, no. 2, pp. 73–85, 1986.

[32] J. Synnevag, A. Austeng, and S. Holm, "Minimum variance adaptive beamforming applied to medical ultrasound imaging," in *Proc. IEEE Ultrason. Symp.*, Sep. 2005, pp. 1199–1202.

[33] M.-X. Tang, N. Kamiyama, and R. J. Eckersley, "Effects of nonlinear propagation in ultrasound contrast agent imaging," *Ultrasound Med. Biol.*, vol. 36, no. 3, pp. 459–466, 2010.

[34] J. Udesen and J. A. Jensen, "Investigation of transverse oscillation method," *IEEE Trans. Ultrason., Ferroelect., Freq., Control*, vol. 53, no. 5, pp. 959–971, May 2006.

[35] M. E. Anderson and G. E. Trahey, "A seminar on *k*-space applied to medical ultrasound," Dept. Biomed. Eng., Duke Univ., Durham, NC, USA, Tech. Rep., 2000. [Online]. Available: http://folk.ntnu.no/htorp/Undervisning/MEDT8007/litteratur/KspaceSeminar.Trahey.pdf

[36] A. Stanziola and M. Tang, "Temporal and spatial processing of high frame-rate contrast enhanced ultrasound data," in *Proc. 21st Eur. Symp. Ultrasound Contrast Imag.*, Jan. 2016, pp. 160–162.

[37] J. Shin, Y. Chen, M. Nguyen, and J. T. Yen, "Robust ultrasonic reverberation clutter suppression using multi-apodization with cross-correlation," in *Proc. IEEE Int. Ultrason. Symp. (IUS)*, Sep. 2014, pp. 543–546.

[38] J. Shin and J. T. Yen, "Clutter suppression using Phase Apodization with Cross-correlation in ultrasound imaging," in *Proc. IEEE Int. Ultrason. Symp. (IUS)*, Sep. 2013, pp. 793–796.

[39] J. Capon, "High-resolution frequency-wavenumber spectrum analysis," *Proc. IEEE*, vol. 57, no. 8, pp. 1408–1418, Aug. 1969.